PAPER

Check for updates

Lignin-derivable, thermally healable thiol-acrylate vitrimers with improved mechanical performance and reprocessability *via* transesterification†

Yu-Tai Wong, [ID] [a] Jignesh S. Mahajan, [ID] [b] Stephanie Synnott [ID] [b] and LaShanda T. J. Korley [ID] ★[ab]

The development of vitrimers with dynamic covalent bonds enables reprocessability in crosslinked networks, offering a sustainable alternative to conventional thermosets. In this work, a thiol-acrylate vitrimer was synthesized from lignin-derivable (bis)phenols (guaiacol and bisguaiacol F) and compared to a control derived from petroleum-based precursors (phenol and bisphenol F) to investigate the effect of structural differences on network properties and thermal reprocessing. The presence of methoxy groups in the lignin-derivable vitrimer promoted intermolecular interactions by serving as additional hydrogen bonding acceptors during curing, leading to a denser network, as evidenced by a higher rubbery storage modulus (~2.4 MPa *vs.* ~1.4 MPa) and glass transition temperature (~34 °C *vs.* ~28 °C). The lignin-derivable vitrimer exhibited a slightly higher elongation-at-break (~170% *vs.* ~130%) and improved mechanical robustness, including a nearly two-fold increase in Young's modulus (~6.9 MPa *vs.* ~3.4 MPa) and toughness (~750 kJ m^{-3} *vs.* ~390 kJ m^{-3}). The similar stress relaxation behavior and activation energy of viscous flow indicated comparable bond exchange dynamics between the two vitrimers, while the lignin-derivable system demonstrated higher thermal healing efficiency with improved recovery of tensile properties after reprocessing. These findings highlight the potential of lignin-based aromatics in designing mechanically robust and sustainable vitrimers, aligning with efforts to develop renewable and reprocessable polymeric materials.

Sustainability spotlight

The end-of-life option for conventional thermosets is generally limited due to their incalcitrant, covalently crosslinked structure. To tackle this challenge, imparting dynamic chemistry could enable reprocessability that promotes life cycle management for thermosets. Incorporating renewable precursors, such as lignin-derivable aromatics, further enhances sustainability. In this study, a thiol-acrylate vitrimer was synthesized using lignin-derivable (bis)phenols, leveraging methoxy groups as additional hydrogen bonding acceptors. The resulting vitrimer exhibited superior mechanical properties, comparable bond exchange dynamics, and higher thermal healing efficiency than its petroleum-based counterpart. This work highlights the potential of lignin-derivable vitrimers in advancing sustainability by reducing reliance on non-renewable resources and promoting circularity of thermosets, aligning with the UN's Sustainable Development Goal 12 (responsible consumption and production).

Introduction

(Meth)acrylate thermosets are widely utilized in coatings and composite applications due to their relatively low cost, rapid curing, and tunable properties (*e.g.*, mechanical strength and glass transition temperature).[1–4] However, these thermosets are challenging to reprocess/recycle due to their covalently cross-linked structure.[5–7] Additionally, aromatic-based (meth)acrylate thermosets are preliminary derived from petroleum-based (bis) phenols (bisphenol A [BPA] and bisphenol F [BPF]), and there are several safety concerns associated with these commercial bisphenols.[8–10] For example, BPA and BPF are suspected endocrine disruptors.[8–10] Together, these challenges highlight the need for alternative strategies that tackle both ends of the life cycle for thermosets: (1) the renewability of feedstock sources, and (2) end-of-life management, while addressing concerns related to sustainability and health impacts.

Lignin-derivable building blocks have since emerged as a sustainable alternative to petroleum-based aromatics, leveraging the aromaticity and abundance of lignin feedstock as an underutilized biomass waste stream.[11] Lignin constitutes around 20–25 wt% of lignocellulosic biomass.[12] Around 100 Mt

[a]Department of Chemical and Biomolecular Engineering, University of Delaware, Newark, Delaware 19716, USA. E-mail: lkorley@udel.edu

[b]Department of Materials Science and Engineering, University of Delaware, Newark, Delaware 19716, USA

† Electronic supplementary information (ESI) available. See DOI: https://doi.org/10.1039/d5su00182j

per year of lignin is separated as a byproduct of the pulp and paper industry.[12] Although bulk lignin has been applied as polymer precursors and fillers for composite applications, the resultant materials can lead to inconsistent thermal/mechanical properties due to lignin's inherent structural heterogeneity.[13–15] Additionally, the materials generated from lignin possess dark color/odor issues.[13–15] To overcome these challenges, bulk lignin can be deconstructed (*via* catalytic/pyrolytic pathways) into small phenolic molecules that are subsequently converted into renewable bisphenols.[16–18] While lignin-derivable (bis)phenols, such as bisguaiacols and bissyringols, share structural similarities with petroleum-based analogues, studies have shown they may offer improved safety—exhibiting reduced estrogenic activity and genotoxicity compared to BPA and BPF—due to the presence of methoxy groups on the aromatic rings, as supported by computational modeling and *in vitro*/*in vivo* evaluations.[19–21] In addition to their lower toxicity, the inherent methoxy groups on aromatic rings have been reported as a handle to promote intermolecular hydrogen bonding with hydrogen bonding donors (*i.e.*, –OH and –NH) in the polymer backbone.[22,23] Previous studies of non-isocyanate polyurethanes (NIPUs) synthesized from lignin-derivable bisphenols have demonstrated enhanced toughness and elongation-at-break (ε_b) due to these additional hydrogen bonding sites.[22,23] The structural similarity to petroleum-based counterparts has also enabled these lignin-derivable (bis)phenols to exhibit comparable thermomechanical properties in (meth)acrylate thermosets, including glass transition temperature (T_g) and storage modulus (E'), providing uncompromised material performance.[24–30] In addition to material performance advantages, recent studies on the cradle-to-gate, life-cycle assessment (LCA) of lignin-based biorefineries have demonstrated reduced environmental impacts compared to traditional petrochemical pathways.[31,32] Sensitivity analyses further indicated that such lignin valorization strategies offer improved environmental performance, particularly in terms of lower global warming potential, when benchmarked against conventional production methods.[33] These findings herein present promising design strategies to synthesize high-performance (meth)acrylate networks using the platform of lignin-derivable (bis)phenols to overcome the sustainability issue of feedstocks.

To further address the sustainability challenge of end-of-life management, circularity, a concept that underscores the reuse of waste products, has gained growing interest in extending the lifecycle of covalently crosslinked (meth)acrylates in addition to the promotion of feedstock renewability.[6,34] One promising strategy involves incorporating dynamic covalent chemistry to impart reprocessability while maintaining the structural integrity of crosslinked networks.[35–38] Vitrimers, which rely on associative bond exchange, have been extensively studied in this context due to their ability to retain crosslink density after dynamic bond exchange.[39,40] Among various associative dynamic chemistries, transesterification has been widely applied in (meth)acrylate-based vitrimers due to its well-established reaction mechanisms and tunable kinetics.[41] Recent studies highlighted a UV-curable, aromatic-based thiol-acrylate vitrimer system leveraging transesterification to exhibit tunable thermal healing by controlling network chemistry.[42–44]

However, challenges remain in vitrimer systems regarding the design of mechanically robust networks without sacrificing reprocessability. For example, conventional ways to improve the mechanical strength and toughness of thermosets, such as increasing crosslink density and incorporating nanofillers, have led to slower stress relaxation times at the reprocessing temperature for transesterification vitrimers due to the lower network mobility inhibiting bond exchange.[45–47] To address these tradeoffs, incorporating non-covalent interactions, such as hydrogen bonding, has been explored to form sacrificial bonds that enhance toughness at the working temperature while preserving the network dynamics by enabling dissociation at elevated reprocessing temperatures.[48] The continued reliance on petroleum-based feedstocks to synthesize transesterification vitrimers is another hurdle that inhibits the overall sustainability of such reprocessable materials. Altogether, leveraging lignin-derivable (bis)phenols to design transesterification vitrimers offers a promising approach toward mechanically robust, sustainable, and reprocessable networks, in which the methoxy groups on aromatic rings could be harnessed to promote intermolecular hydrogen bonding without compromising reprocessability.

Herein, we propose the design of a thiol-acrylate vitrimer synthesized from lignin-derivable (bis)phenols (guaiacol and bis-guaiacol F [BGF]) and its counterpart synthesized using petroleum-based precursors (phenol and BPF) as the control, which differs only in the presence of methoxy substituents on the aromatic rings, to investigate the effect of the structural handle on network properties. In this vitrimer design, we incorporate a diglycidyl acrylate to impart mechanical rigidity and a glycidyl acrylate to lower the viscosity of the monomer mixture. A tetrafunctional thiol is used as the crosslinker to participate in the step-growth radical thiol-acrylate reaction in parallel to the acrylate–acrylate, chain-growth reaction, and to subsequently suppress the network inhomogeneity induced by the acrylate homopolymerization.[42] A small amount of organic phosphoric acid methacrylate is incorporated as the transesterification catalyst, following literature protocols.[42] The chemical structures of each component used in the two vitrimers are shown in Scheme 1. The resulting vitrimers with free hydroxyl groups on the polymer backbone can be leveraged to form hydrogen bonds with carbonyl or methoxy substituents and are expected to undergo thermally activated transesterification with the neighboring ester group (Scheme 1). It is important to note that the primary goal of this relatively complex formulation is to create a liquid resin that facilitates film fabrication. However, the system can be simplified by removing the monofunctional glycidyl acrylate and replacing the methacrylate-based catalyst with organometallic complexes, thereby minimizing complications from chain reptations associated with these species during bond exchange events for more refined studies of bond exchange dynamics. In this work, we aim to investigate two thiol-acrylate vitrimers that differ in the presence of methoxy substituents on aromatic rings to probe the impact of hydrogen bonding and facilitate an understanding of the interplay between network architecture (gel fraction, T_g, and rubbery storage modulus), mechanical performance (Young's modulus, toughness, and ε_b), bond exchange dynamics (stress-relaxation times),
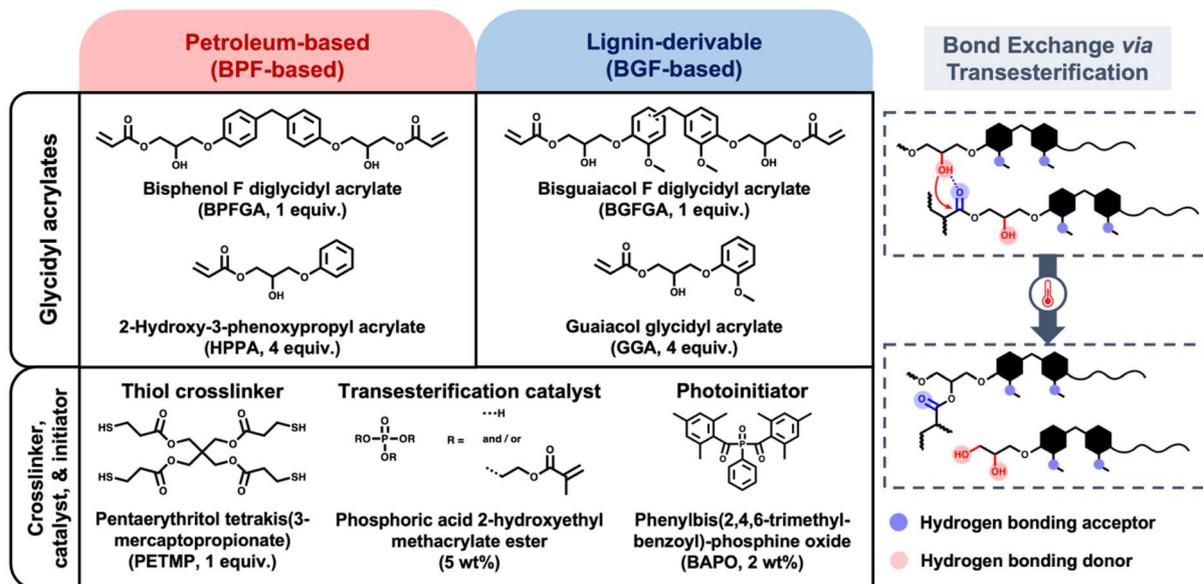
Scheme 1 Chemical structures of each component used in synthesizing vitrimers (left) and the bond exchange pathway *via* transesterification (right).

and reprocessability. Specifically, reprocessability was assessed by the recovery ratio of each tensile metric for vitrimers after thermal healing. Finally, our findings demonstrate how lignin-derivable feedstocks can unlock new molecular insights into the design of vitrimers with key performance advantages.

Experimental

Materials

Ethyl acetate (≥99.9%), toluene (≥99.5%), hexanes (99%), sodium chloride (≥99.5%), dichloromethane (DCM; ≥99.5%), sodium hydroxide (NaOH; ≥98.7%), and potassium hydroxide (KOH; ≥85.0%) were purchased from Fisher Scientific. Vanillyl alcohol (≥98%), guaiacol (≥99%), Amberlyst® 15 hydrogen form (dry; MQ200), inhibitor removers, phenylbis(2,4,6-trimethylbenzoyl)phosphine oxide (BAPO; 97%), pentaery-thritol tetrakis(3-mercaptopropionate) (PETMP; ≥95%), phosphoric acid 2-hydroxyethyl methacrylate ester (90%), 2-hydroxy-3-phenoxypropyl acrylate (HPPA; ≥80%), and acrylic acid (99%) were purchased from Sigma-Aldrich. Deuterated chloroform (CDCl$_3$; ≥99.75%), deuterated dimethyl sulfoxide (DMSO-d_6; ≥99.5%), acetonitrile (≥99.7%), and *n*-butyldimethyl-chlorosilane (96%) were purchased from Thermo Fisher Scientific. Epichlorohydrin (≥99%) and tetrabutylammonium bromide (TBAB; ≥99%) were purchased from Acros Organics. Bisphenol F (BPF) diglycidyl ether (EPON™ 862) was purchased from Westlake Epoxy. Ar (grade 5) and N$_2$ (liquid) were purchased from Keen Compressed Gas. All chemicals were used as received except for HPPA, which was destabilized by mixing with inhibitor removers for 1 h and filtered before use.

Synthesis of bisguaiacol F (BGF)

BGF was synthesized as described in the literature (Scheme S1a†).[18,22,23] Vanillyl alcohol (5 g, 1.0 equiv.) and guaiacol (16 g,

4.0 equiv.) were mixed in a single-neck, round-bottom flask equipped with a magnetic stir bar. The reaction mixture was stirred and heated at 75 °C with an Ar sparge until all solids were dissolved. The solid catalyst, Amberlyst® 15 hydrogen form (30% w/w relative to vanillyl alcohol), was subsequently added to the reaction mixture, which was allowed to react for 12 h. The reaction mixture was then cooled to ~20 °C, dissolved in ethyl acetate, and filtered to remove all solid catalysts. The filtrate was washed with saturated brine solution three times in a separatory funnel. The organic phase was collected, and excess ethyl acetate was removed by rotary evaporation. The residue was passed through an automated flash column chromatograph (Biotage® Selekt, Sfär Silica Column—60 μm particle size, 100 Å pore size, 100 g silica gel) with a step gradient of ethyl acetate (33% v/v) and hexanes (67% v/v) as the mobile phase to purify the product. Excess hexanes and ethyl acetate were removed by rotary evaporation and recovered for use in the washing step. The product was dried under vacuum at 50 °C for 12 h to yield BGF as a white solid (purity: >99%, yield: ~54 mol%). Proton (^{1}H) nuclear magnetic resonance (NMR) (400 MHz, CDCl$_3$, 16 scans, 25 °C): δ 6.85–6.64 (m, 6H), 5.48 (s, 2H), 3.85–3.83 (m, 8H). Fourier transform mass spectrometry (FTMS) (electrospray ionization [ESI], *m/z*): calculated for C$_{15}$H$_{16}$O$_4$ 260.1049; found 260.1041. The ^{1}H NMR spectrum with peak assignments is shown in Fig. S1.†

General procedure for the synthesis of (di)glycidyl ethers

Guaiacol glycidyl ether and BGF diglycidyl ether were synthesized by following the steps described in the literature (Scheme S1b†).[18,22,23] Guaiacol/BGF (2 g/4 g, 1.0 equiv.), epichlorohydrin (11 g, 7.0 equiv. for guaiacol and 14 g, 10.0 equiv. for BGF), and TBAB (0.1 equiv.) were mixed in a single-neck, round-bottom flask equipped with a magnetic stir bar and then sparged with Ar gas for 30 min at ~20 °C under constant stirring. The mixture

was then heated at 50 °C for 2 h and cooled in an ice bath at ~0 °C for 15 min. 40 wt% aqueous NaOH (4.0 equiv.) was dropwise added to the cooled reaction mixture, and the reaction proceeded at 20 °C for 18 h in a water bath. The reaction mixture was then dissolved in ethyl acetate and washed with saturated brine solution at least three times in a separatory funnel until the aqueous phase approached neutral pH. The organic phase was collected, and excess ethyl acetate was removed by rotary evaporation. The residue was passed through an automated flash column chromatograph (Biotage® Selekt, Sfär Silica Column—60 μm particle size, 100 Å pore size, 100 g silica gel) with a step gradient of ethyl acetate (60% v/v) and hexanes (40% v/v) as the mobile phase to purify the product. Excess hexanes and ethyl acetate were removed by rotary evaporation and recovered for use in the washing step. The products were dried under vacuum at 50 °C for 24 h.

Guaiacol glycidyl ether. Yellow transparent liquid (purity: >99%, yield: ~86 mol%). ^{1}H NMR (400 MHz, CDCl$_3$, 16 scans, 25 °C): δ 6.98–6.87 (m, 4H), 4.24 (dd, J = 11.4, 3.6 Hz, 1H), 4.05 (dd, J = 11.4, 5.5 Hz, 1H), 3.87 (s, 3H), 3.41–3.37 (m, 1H), 2.89 (dd, J = 5.0, 4.1 1H), 2.74 (dd, J = 4.9, 2.6 Hz, 1H). FTMS (ESI, m/z): calculated for C$_{10}$H$_{12}$O$_3$ 181.0820; found 181.0866. The ^{1}H NMR spectrum with peak assignments is shown in Fig. S2.†

BGF diglycidyl ether. White solid (purity: >99%, yield: ~80 mol%). ^{1}H NMR (400 MHz, DMSO-d_6, 16 scans, 25 °C): δ 6.79 (m, 6H), 4.22 (ddd, J = 11.4, 7.0, 2.7 Hz, 2H), 3.75 (m, 10H), 3.29 (m, 2H), 2.71 (m, 4H). FTMS (ESI, m/z): calculated for C$_{21}$H$_{24}$O$_6$ 373.1606; found 373.1658. The ^{1}H NMR spectrum with peak assignments is shown in Fig. S3.†

General procedure for the synthesis of (di)glycidyl acrylates

Guaiacol glycidyl acrylate (GGA) and BPF/BGF diglycidyl acrylates (BPFGA/BGFGA) were synthesized by following the steps described in the literature (Scheme S1c†).[49] KOH (0.1 equiv. for guaiacol glycidyl ether and 0.15 equiv. for BPF/BGF diglycidyl ether) was slowly dissolved in acrylic acid (2.0 equiv. for guaiacol glycidyl ether and 3.0 equiv. for BPF/BGF diglycidyl ether) to prevent overheating from the exothermic mixing, and then the solution was added to the mixture of (di)glycidyl ether (2.5 g, 1.0 equiv. of guaiacol glycidyl ether or BPF/BGF diglycidyl ether), hydroquinone (0.1 equiv.), and toluene (0.3 M relative to (di)glycidyl ether) in a single-neck, round-bottom flask equipped with a magnetic stir bar. The reaction mixture was heated at 90 °C and reacted for 7 h under constant stirring. After reaction completion, toluene was first removed by rotary evaporation, and the residue was then dissolved in ethyl acetate. The mixture was washed with a saturated brine solution at least three times in a separatory funnel until the aqueous phase approached neutral pH. The organic phase was collected, and excess ethyl acetate was removed by rotary evaporation. The residue was passed through an automated flash column chromatograph (Biotage® Selekt, Sfär Silica Column—60 μm particle size, 100 Å pore size, 100 g silica gel) with ethyl acetate and hexanes as the mobile phase to purify the product. Excess hexanes and ethyl acetate were removed by rotary evaporation and recovered for use in the washing step. The products were dried under vacuum at ~20 °C for 48 h.

GGA. Purified by flash column chromatography with a step gradient of ethyl acetate (50% v/v) and hexanes (50% v/v). Yellow transparent liquid (purity: ~96%, yield: ~50 mol%). ^{1}H NMR (400 MHz, CDCl$_3$, 16 scans, 25 °C): δ 6.94 (m, 4H), 6.44 (m, 1H), 6.17 (m, 1H), 5.87 (ddd, J = 10.4, 3.7, 1.4 Hz, 1H), 4.20 (m, 5H), 3.85 (d, 4.4 Hz, 3H). FTMS (ESI, m/z): calculated for C$_{13}$H$_{16}$O$_5$ 253.1031; found 253.1080. The ^{1}H NMR spectrum with peak assignments is shown in Fig. S4.†

BPFGA. Purified by flash column chromatography with a step gradient of ethyl acetate (75% v/v) and hexanes (25% v/v). Yellow transparent oil (purity: ~95%, yield: ~52 mol%). ^{1}H NMR (400 MHz, CDCl$_3$, 16 scans, 25 °C): δ 6.97 (m, 8H), 6.43 (m, 2H), 6.14 (m, 2H), 5.85 (m, 2H), 4.13 (m, 10H), 2.77 (m. 2H). FTMS (ESI, m/z): calculated for C$_{25}$H$_{28}$O$_8$ 457.1818; found 457.1877. The ^{1}H NMR spectrum with peak assignments is shown in Fig. S5.†

BGFGA. Purified by flash column chromatography with a step gradient of ethyl acetate (85% v/v) and hexanes (15% v/v). Orange transparent oil (purity: ~95%, yield: ~57 mol%). ^{1}H NMR (400 MHz, CDCl$_3$, 16 scans, 25 °C): δ 6.76 (m, 6H), 6.43 (m, 2H), 6.16 (ddd, J = 17.3, 10.4, 5.7 Hz, 2H), 5.86 (dd, J = 10.4, 1.5 Hz, 2H), 4.15 (m, 10H), 3.82 (m, 8H). FTMS (ESI, m/z): calculated for C$_{27}$H$_{32}$O$_{10}$ 517.2029; found 517.2092. The ^{1}H NMR spectrum with peak assignments is shown in Fig. S6.†

Preparation of thiol-acrylate vitrimers

BPF-based and BGF-based thiol-acrylate vitrimers were photopolymerized *via* the radical acrylate–acrylate chain-growth and radical thiol-acrylate step-growth polymerization of the following monomer mixtures (Scheme 1). On a basis of 1 g of monomer formulation, 1 equiv. of diglycidyl acrylate (250 mg for BPF-based and 258 mg for BGF-based), 4 equiv. of glycidyl acrylate (489 mg for BPF-based and 505 mg for BGF-based), 1 equiv. of thiol crosslinker (PETMP) (261 mg for BPF-based and 237 mg for BGF-based), 5 wt% of transesterification catalyst (phosphoric acid 2-hydroxyethyl methacrylate ester), 2 wt% of photoinitiator (BAPO), and 2.5 mL of ethyl acetate were mixed in a scintillation vial. The vial containing the monomer solution was then covered with aluminum foil to prevent early termination with a slight opening for solvent vapor to vent in a fume hood for 48 h. A mold was fabricated using two *n*-butyldimethylchlorosilane treated microscope slides (25 mm × 75 mm × 1 mm) with plastic shims (0.25 mm thick) sandwiched in between using binder clips to create thickness-controlled spacers for film preparation. The monomer solution was transferred to the space between slides using a Pasteur pipette. Films were subsequently cured in an ultraviolet (UV) chamber (SPDI UV, λ = 365 nm) at an intensity of ~13 mW cm^{-2} for 20 min. After photocuring, the films were peeled off from the slides and transferred to a PTFE evaporating dish. These films were then subjected to a thermal post-cure at 120 °C in an oven for an additional 3 h to ensure maximum conversion. The temperature for thermal post-curing was determined by the exothermic peaks in differential scanning calorimetry (DSC) (Fig. S7†). Rectangular films were obtained as molded from the

microscope slides with dimensions of 25 mm × 10 mm × 0.25 mm (length × width × thickness) for further characterization. All specimen films were kept in a desiccator containing Drierite prior to any characterization experiments to avoid absorption of water from the atmosphere that would potentially influence the transesterification kinetics. The water uptake profile is summarized in Fig. S8.†

Thermal healing

As-prepared sample films were cut in half, and the separated pieces were placed together with the cut sections in direct contact. To maintain alignment and control thickness, the films were sandwiched between Teflon sheets with plastic shims (0.25 mm thick) as spacers and clamped using binder clips. Microscope slides were placed on the outer layers to prevent bending during the process. The assembled samples were then placed in an oven at 100 °C under air for varying times to allow thermally activated healing prior to the evaluation via tensile testing.

Soxhlet extraction

The gel fractions of cured films before and after thermal post-curing were probed via Soxhlet extraction. The films were weighed to obtain the initial mass (m_0) before the extraction. The extraction was set up for 24 h with a single extracting cycle duration ~10 min at 60 °C using 250 mL of DCM as the extraction solvent. The films were weighed again after drying in an oven at ~20 °C under vacuum for 24 h to obtain the final mass (m_f). The gel fractions were calculated as m_f/m_0. All samples were extracted in triplicate, and reported values are the average gel fractions with the standard deviation as the error.

^{1}H NMR spectroscopy

^{1}H NMR samples were prepared either in DMSO-d_6 or CDCl$_3$ and analyzed using a Bruker Neo 400 MHz (5-mm BBFO probe) spectrometer. Spectra processing and analysis were conducted using the MestReNova software package.

Mass spectroscopy

The exact masses of BGF, (di)glycidyl ethers, and (di)glycidyl acrylates were measured by ESI-FTMS using a Q-Exactive Orbitrap (Thermo Fisher Scientific) mass spectrometer. Prior to the analysis, the samples were dissolved in acetonitrile at a concentration of 0.1 mg mL^{-1}. Direct syringe injection of the samples into the mass spectrometer was conducted in a positive ion mode for ESI-FTMS.

DSC

A Discovery DSC (TA Instruments) was used to determine the temperature for thermal post-curing. Each sample was encapsulated in a Tzero aluminum pan sealed with the corresponding Tzero lid. Two heating and one cooling cycles were performed between −50 and 150 °C under a continuous N$_2$ flow (50 mL min^{-1}) at a rate of 10 °C min^{-1}. The temperature where the

exothermic peak occurred was identified as an additional curing temperature. DSC curves are presented in Fig. S7.†

In situ near-infrared (NIR) spectroscopy

In situ NIR spectroscopy was performed using a Nicolet iS50 FT-IR spectrometer (Thermo Fisher Scientific) with a nitrogen-cooled MCT detector. Real-time change of functional group conversion was monitored as the peak area decrease of C–H from the acrylate group (6100–6200 cm^{-1}) and S–H from the thiol group (2500–2600 cm^{-1}). The spectra were collected over 16 scans s^{-1} with a 4 cm^{-1} resolution under 365 nm light irradiation at an intensity of ~13 mW cm^{-2}. Both vitrimers were measured in triplicate, and reported values are the average conversions of the triplicate.

Attenuated total reflectance-Fourier transform infrared (ATR-FTIR) spectroscopy

ATR-FTIR spectroscopy was performed using a Thermo Nicolet NEXUS 870 FTIR with a deuterated triglycine sulfate/potassium bromide (DTGS/KBr) detector. All acrylate network films were scanned (128 scans) at a resolution of 4 cm^{-1} in the wavenumber range of 400–4000 cm^{-1}.

Thermogravimetric analysis (TGA)

A Discovery TGA (TA Instruments) was used to study the thermal stability of the vitrimers. Each sample was placed in a 100 μL platinum pan. All samples were heated to 700 °C from ~20 °C at a heating rate of 10 °C min^{-1} under a continuous N$_2$ flow (50 mL min^{-1}). The temperature at 5 wt% loss ($T_{d5\%}$) was used to assess the thermal stability. TGA curves are presented in Fig. S9† and summarized in Table S1.†

Dynamic mechanical analysis (DMA)

An RSA-G2 Solids Analyzer (TA Instruments) was used to investigate the thermomechanical properties and stress-relaxation behavior. A temperature ramp was applied to rectangular films (25 mm × 3 mm × 0.25 mm [length × width × thickness]) to investigate storage modulus (E'), loss modulus (E''), and tan δ (E''/E') of each specimen using oscillatory tension mode heated from −25 to 100 °C at a rate of 3 °C min^{-1} with a strain amplitude of 1% and frequency of 1 Hz. All samples were tested in triplicate, and reported values are the average numbers with the standard deviation as the error. Stress-relaxation measurements were performed using the tensile geometry to probe the stress-relaxation profile of vitrimers at 85, 90, 100, and 110 °C, respectively. Rectangular films (25 mm × 3 mm × 0.25 mm [length × width × thickness]) were subjected to a strain amplitude of 2% to record the change of elastic modulus over time. Characteristic relaxation times (τ^*) were determined as the time when the elastic modulus reaches 1/e of the initial value. All samples were tested in triplicate, and reported values are the average numbers with the standard deviation as the error.

Tensile testing

Tensile properties of the vitrimers were measured on a Zwick/Roell tensile tester with a load cell of 100 N and a clamp force of 200 N at ∼20 °C. The films used for the test were cut into a dog bone shape based on the standard test method ASTM D1708, with the dimensions scaled down by a factor of 2. All samples were subjected to an extension strain rate of 10% min^{-1} until film failure. The reported values of Young's modulus (E_t), elongation-at-break (ε_b), ultimate tensile strength (σ_m), and toughness (determined by the area under the stress–strain curve) are the average of triplicate measurements with the standard deviation as the error.

Results and discussion

In this study, we designed petroleum-based (phenol- and BPF-based) and lignin-derivable (guaiacol- and BGF-based) thiol-acrylate vitrimers that differ only in the presence of methoxy groups on the aromatic rings. This structural variation allows us to systematically investigate the impact of the methoxy groups on network formation, network architecture, thermomechanical properties, mechanical performance, and bond exchange dynamics. By comparing these vitrimer properties, we aim to establish key structure–property relationships that will enable end-of-life management while maintaining performance requirements. The discussion of these networks in the later sections includes comparisons of the vitrimers before and after thermal post-curing, while all other results shown are conducted on thermally post-cured vitrimers unless otherwise specified.

Preparation of thiol-acrylate vitrimers

In situ NIR spectroscopy was used to monitor the real-time conversion of acrylate and thiol groups during UV curing in the wavenumber ranges of 6100–6200 cm^{-1} and 2500–2600 cm^{-1}, respectively. The experiments were conducted under the same light source wavelength (365 nm) and intensity (13 mW cm^{-2}) as the UV chamber used for vitrimer sample preparation to replicate

curing conditions. Both BPF- and BGF-based vitrimers achieved nearly complete acrylate conversion and ∼45% thiol conversion as shown in Fig. 1. The nearly complete acrylate conversion was expected due to the multiple propagation pathways available to acrylate groups, including chain-growth homopolymerization of acrylates and step-growth thiol-acrylate polymerization, while the unconsumed thiol group is attributed to the competition between these pathways.[50,51] Additionally, the observed thiol conversion aligns with the predicted stoichiometric acrylate/thiol ratio of 3/2.[50] The real-time conversion data indicate that the incorporation of methoxy groups on the aromatic rings has no significant effect on the final conversion as long as sufficient curing time is provided. Based on these findings, our vitrimer preparation protocol was established, consisting of 20 min of UV curing followed by 3 h of thermal post-curing at 120 °C to ensure no additional curing will take place in the later characterization studies at elevated temperatures. The temperature used for thermal post-curing was determined by the exothermic peak that appeared on the first heating cycle of the UV-cured sample in DSC, as shown in Fig. S7.† This result further showcases the rapid curing kinetics of thiol-acrylate systems and their potential compatibility with diverse options of manufacturing processes.
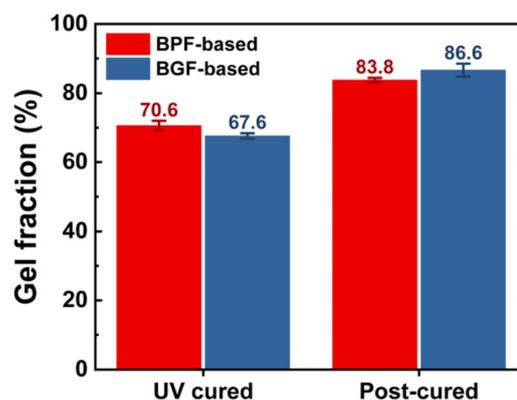

Fig. 2 Gel fraction comparison before and after thermal post-curing at 120 °C for 2 h obtained by Soxhlet extraction.
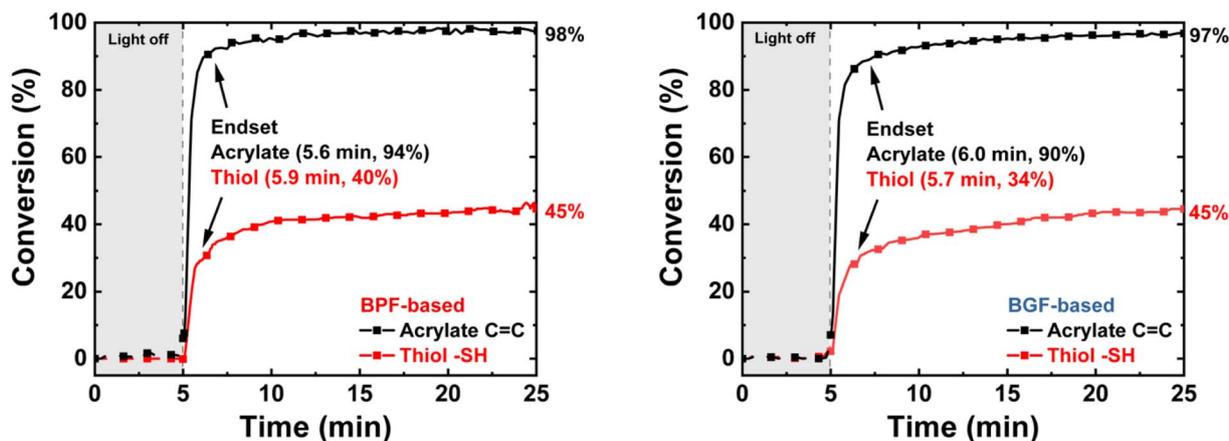

Fig. 1 Real-time UV curing conversion profiles of BPF-based and BGF-based vitrimers obtained from *in situ* NIR spectroscopy (under 365 nm light irradiation at an intensity of ∼13 mW cm^{-2}).

Table 1 Gel fraction and volume change before and after thermal post-curing at 120 °C for 2 h

Sample	Gel fraction (%)		Volume change[a]		
	UV cured	Post-cured	D_{before} (g cm^{-3})	D_{after} (g cm^{-3})	ΔV (%)
BPF-based	70.6 ± 1.4	83.8 ± 0.6	1.29 ± 0.04	1.32 ± 0.04	−1.9 ± 0.3
BGF-based	67.6 ± 0.8	86.6 ± 1.9	1.30 ± 0.03	1.31 ± 0.03	−0.9 ± 0.3

[a] Density is derived from weighing a rectangular specimen in the dry state and calculating the volume from its measured dimensions. Reported values are the average of triplicate measurements, with the error indicated by the standard deviation.

Network structures and thermomechanical properties

Gel fraction measurements before and after thermal post-curing were used to evaluate the evolution of network formation and the maximum degree of crosslinking achieved in each vitrimer (Fig. 2 and Table 1). Both vitrimers showed an increase in gel fraction after post-curing (∼71% to ∼84% for BPF-based and ∼68% to ∼87% for BGF-based), indicating additional curing during the thermal treatment. It is noted that the BGF-based vitrimer, which contains methoxy groups on the aromatic rings, exhibited a slightly higher increase (∼19%) in gel fraction compared to the BPF-based vitrimer (∼13%). This difference may suggest stronger intermolecular interactions that bring polymer chains into closer proximity, facilitating further reactions between unreacted groups. To test this hypothesis, density measurements were performed before and after thermal post-curing to quantify volume shrinkage; a smaller shrinkage would indicate reduced intermolecular distance during curing due to stronger interactions between monomers and polymer chains.[52] Values of the densities and the extent of volume change are summarized in Table 1. The BGF-based vitrimer exhibited similar volume shrinkage (∼0.9%) to the BPF-based vitrimer (∼1.9%) during thermal post-curing, indicating negligible differences in intermolecular interactions and suggesting that only minimal additional curing occurred locally during this step.

The thermomechanical properties of the thermally post-cured vitrimers, including the storage modulus and T_g, were analyzed using a DMA temperature ramp and are summarized in Table 2. The temperature-dependent transitions in storage modulus and the tan δ curve depicted in Fig. 3a provide insight into polymer chain mobility in response to temperature changes and offer information on the network structure of the vitrimers.

The consistent storage modulus noted in the temperature range above T_g (60–100 °C) is characteristic of associative dynamic chemistry, where bond breaking and bond forming occur simultaneously during the bond exchange event such that the crosslink density remains unchanged.[39,40,53] Notably, the BGF-based vitrimer exhibited a higher storage modulus (∼2.4 MPa) in the rubbery regime (E_r', the storage modulus at T_g + 50 °C) than the BPF-based vitrimer (∼1.4 MPa), as shown in Fig. 3b. According to the theory of rubber elasticity, the higher E_r' of the BGF-based vitrimer suggests a denser network, as E_r' is directly proportional to crosslink density.[54–56] While calculation of crosslink density is dependent on different theoretical models, caution is needed when making direct comparisons based on E_r' alone. To provide a more comprehensive assessment of crosslink density differences, we considered multiple factors in addition to E_r', including volume shrinkage, T_g, and Young's modulus (discussed in a later section), instead of directly quantifying crosslink density values. In contrast, the storage modulus in the glassy state (E_g', the storage modulus at T_g − 30 °C) reflects contributions from chain entanglements and non-covalent interactions. Both vitrimers exhibited similar values of E_g', indicating that their intermolecular interactions reached a comparable state after thermal post-curing. This similar E_g' implies that the promoted hydrogen bonding in the BGF-based vitrimer primarily influenced the early stages of network formation rather than in the fully cured state.

The T_g of each vitrimer was determined from the peak temperature of the tan δ curve, where tan δ is defined as the ratio of E''/E' to denote the transition from the glassy state to the rubbery state. A well-defined peak in the tan δ curve is observed in Fig. 3a, indicating a more homogeneous network architecture in the thiol-acrylate system compared to acrylate-only networks with a high extent of network inhomogeneity.[30,42] Among the two vitrimers, the BGF-based system exhibited a higher T_g (∼34 °C) than the BPF-based system (∼28 °C), indicating a network with more restricted chain mobility, which is consistent with the higher crosslink density inferred from the E_r' analyses.[57]

Table 2 Thermomechanical and tensile properties of BPF- and BGF-based vitrimers

Sample	$E_g'{}^{a}$ (GPa)	$E_r'{}^{b}$ (MPa)	T_g (°C)	$E_t{}^{c}$ (MPa)	ε_b (%)	σ_m (MPa)	Toughness (kJ m^{-3})
BPF-based	3.0 ± 0.3	1.4 ± 0.1	28 ± 1	3.4 ± 1.3	130 ± 11	0.63 ± 0.02	390 ± 20
BGF-based	3.2 ± 0.1	2.4 ± 0.2	34 ± 1	6.9 ± 0.8	170 ± 15	1.13 ± 0.03	750 ± 40

[a] Storage modulus in the glassy state (T_g − 30 °C). [b] Storage modulus in the rubbery state (T_g + 50 °C). [c] Young's modulus was determined by the slope of the initial elastic region (within 1% of strain) from the engineering tensile stress–strain curves.
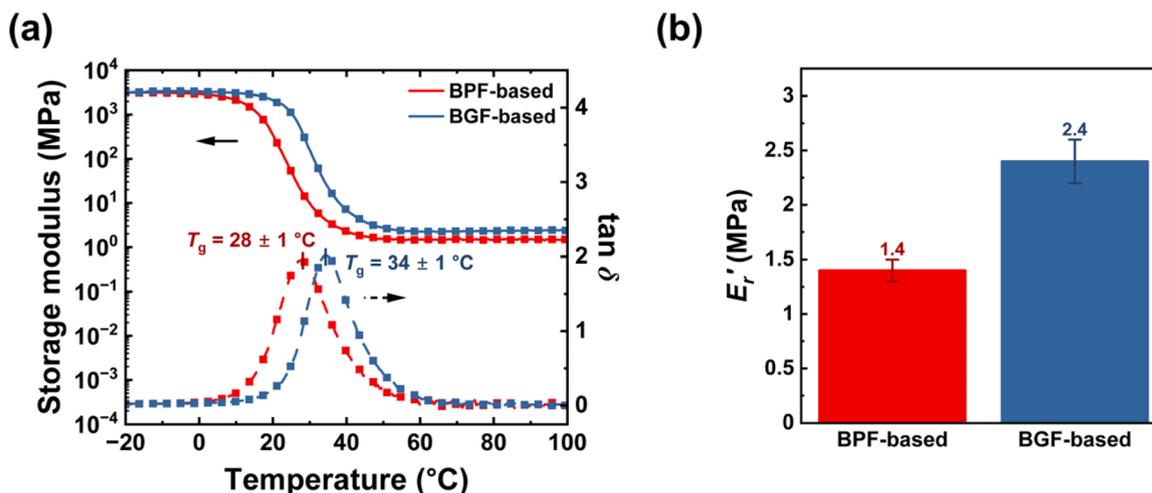
Fig. 3 Thermomechanical properties of thermally post-cured vitrimers: (a) E' (solid line, left y-axis) and tan δ curves (dashed line, right y-axis), and (b) comparison of E_r' at T_g + 50 °C.

Tensile properties of thiol-acrylate vitrimers

The effect of structural differences on mechanical behavior was assessed using uniaxial tensile testing at room temperature (~20 °C) to evaluate the material performance under typical working conditions. The BGF-based vitrimer, in general, exhibited higher mechanical performance reflected by all tensile metrics (*e.g.*, E_t, ε_b, σ_m, and toughness), as summarized in Table 2. As shown in the stress–strain curves in Fig. 4a, the BGF-based vitrimer was more extensible than the BPF-based vitrimer with higher ε_b (~170% *vs.* ~130%). It is also important to note that these tensile tests were conducted at a temperature much lower than the T_g for the BGF-based vitrimer. The effect induced by the difference between T_g and tested temperature is evident from the DMA curve in Fig. 3a, where the E' of the BGF-based vitrimer at the testing temperature (~20 °C) is nearly an order of magnitude higher than the BPF-based vitrimer (~2.0 GPa *vs.* ~0.3 GPa). However, the BGF-based

vitrimer still exhibited a higher elongation-at-break compared to its counterpart, even under these conditions where reduced elasticity is usually expected.

The E_t and toughness of the BGF-based vitrimer (E_t ~ 6.9 MPa and toughness ~750 kJ m^{-3}) were both ~2× that of the BPF-based vitrimer (E_t ~3.4 MPa and toughness ~390 kJ m^{-3}), as shown in Fig. 4b. This increase in E_t is likely due to a combination of factors, including the higher T_g of the BGF-based vitrimer and the potentially higher crosslink density suggested by the network structure and thermomechanical analyses. The higher T_g promotes glassy behavior for the BGF-based vitrimer under tensile testing conditions, while the higher crosslink density leads to reduced deformability and enhanced resistance to applied stress. Additionally, the higher toughness observed in the BGF-based vitrimer correlated with its higher crosslink density and the potential contribution of promoted hydrogen bonding as discussed in the context of network architecture. Evidence of enhanced hydrogen bonding
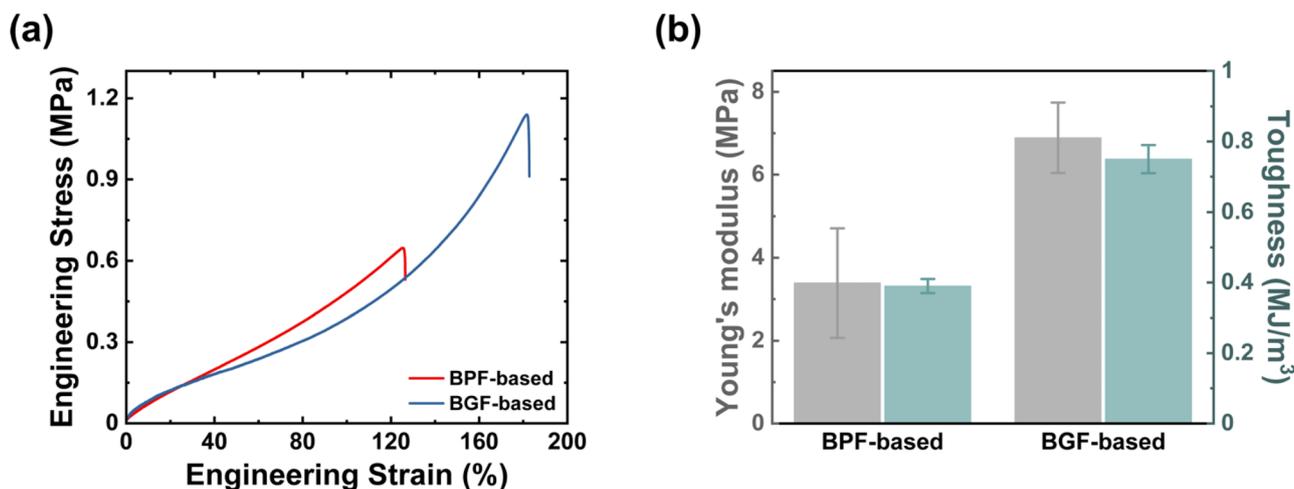

Fig. 4 (a) Representative tensile stress–strain curves and (b) comparison of Young's modulus and toughness of thermally post-cured vitrimers.

can be observed in the ATR-FTIR spectra, where the –OH absorption bands (3200–3700 cm^{-1}) showed a slightly more pronounced shoulder at ~3250 cm^{-1} (Fig. S10†), indicative of a greater proportion of hydrogen-bonded hydroxyl groups.[22,23]

Overall, both the network structure and tensile analyses consistently suggest that incorporating additional methoxy groups into thiol-acrylate vitrimers contributes to a denser network induced by the specific interactions during network formation. This enhanced crosslink density is the driving factor of the improved mechanical robustness for the BGF-based vitrimer.

Bond exchange dynamics

Stress relaxation experiments were conducted at four different temperatures (85, 90, 100, and 110 °C) using a strain amplitude of 2%, ensuring that measurements remained within the linear elastic region. Stress dissipation under constant applied strain was monitored by tracking the decrease in elastic modulus over time to capture the viscoelastic behavior resulting from dynamic bond exchange events and chain segment reptation. It is important to note that the measured relaxation also includes the motion of the transesterification catalyst, which is incorporated into the network structure. To quantify this behavior, characteristic relaxation times (τ^*) were determined as the time required for the modulus to decrease to $1/e$ of its initial value. The relaxation time profiles (Fig. 5a) indicate that both vitrimers exhibit similar relaxation behavior at all tested temperatures, with no statistically significant differences (all p-values > 0.05, Table S2†).

In addition to the relaxation time profile, the topology freezing temperature (T_v) and activation energy of viscous flow (E_a) can also be extracted from the Arrhenius relationship of temperature-dependent τ^*.[37] Relaxation times are related to viscosity via the Maxwell relation, while viscous flow follows the Arrhenius relationship, which is governed by the rate of associative bond exchange at elevated temperatures. Thus, the temperature dependence of the obtained relaxation times was fit to a general Arrhenius equation (eqn (1)):

$$\tau^* = \tau_0 \exp\left(\frac{E_a}{RT}\right) \tag{1}$$

where τ_0 is the relaxation time prefactor and R is the ideal gas constant.[42] Given by the relationship, we can derive the following expression (eqn (2)) to plot Fig. 5b accordingly:

$$\ln(\tau^*) = \ln\tau_0 + \frac{1}{T}\cdot\frac{E_a}{R} \tag{2}$$

The corresponding T_v and E_a values for BPF- and BGF-based vitrimers are provided in Fig. 5b. T_v was defined as the temperature at which network viscosity reaches 10^{12} Pa s; detailed calculations are available in the ESI.† E_a, which quantifies the sensitivity of viscosity to temperature changes, was obtained from the slope of Fig. 5b. T_v serves as an indicator of the temperature at which bond exchange reactions occur at a rate sufficient to enable network rearrangement. The calculated T_v values for both vitrimers (~−19 °C for the BPF-based vitrimer and ~−7 °C for the BGF-based vitrimer) were lower than their respective T_g values, suggesting that their T_g represents the threshold where chain mobility becomes adequate to facilitate a longer range of network rearrangement in this case.[39,40] Additionally, the E_a values of both vitrimers showed no significant difference, indicating that their bond exchange dynamics are comparable.

Surprisingly, the BGF-based vitrimer, which has a higher crosslink density as suggested by thermomechanical and mechanical property analyses, exhibited bond exchange dynamics comparable to its petroleum-based counterpart. A network with higher crosslink density would typically be expected to exhibit slower stress relaxation due to reduced chain mobility.[47,57] However, since both vitrimers possess a similar ratio of dynamic bond exchangeable groups (i.e., hydroxyl and ester groups), the reduced intermolecular distance in the BGF-
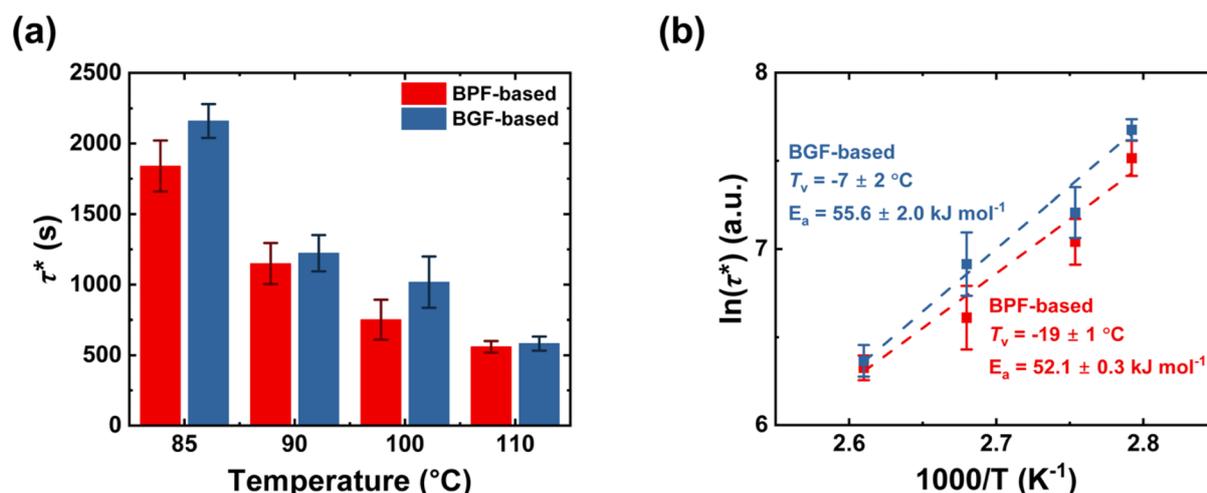

Fig. 5 Network dynamic studies of (a) characteristic stress relaxation time (τ^*) profiles, and (b) Arrhenius relationship between 1000/T and τ^*, where calculated E_a and T_v are presented and reported by their average from triplicate measurements with the standard deviation as the error.
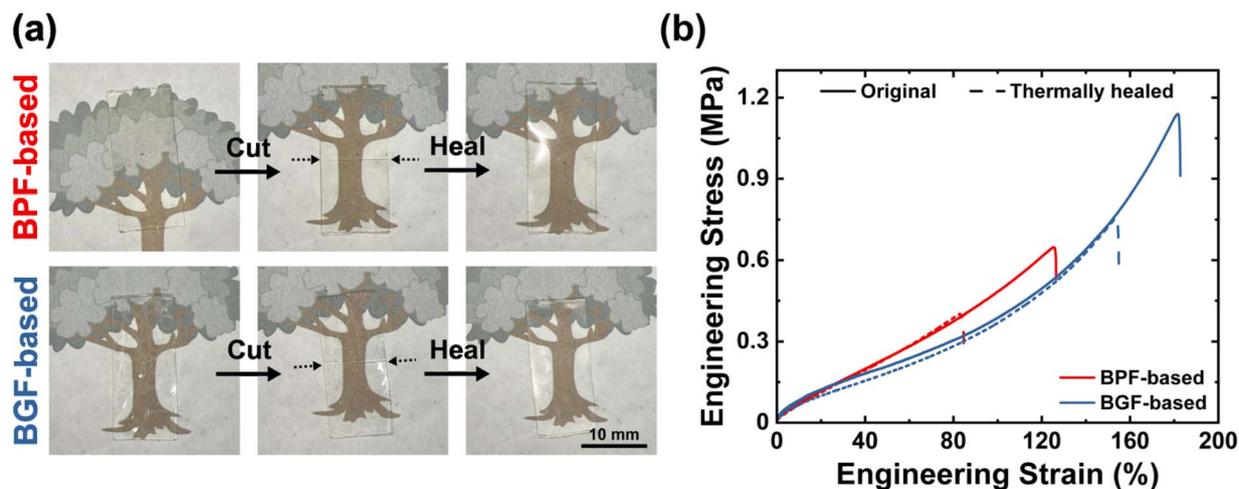
Fig. 6 Thermal healing study of vitrimer films at 100 °C for 24 h shown by: (a) optical images, and (b) representative tensile stress−strain curves after healing.

based vitrimer likely facilitates bond exchange events by increasing the probability of reactive group interactions.[58,59] This structural advantage mitigates the expected mobility loss associated with higher crosslink density. Altogether, the BGF-based vitrimer achieves comparable bond exchange dynamics along with a similar stress relaxation behavior to the BPF-based vitrimer while retaining a more robust network structure.

Reprocessability through thermal healing

The reprocessability of the synthesized thiol-acrylate vitrimers was evaluated based on their ability to recover from damage (*i.e.*, complete cut in the films), followed by healing at 100 °C through thermally activated transesterification (Fig. 6a). To compare the healing efficiency, uniaxial tensile tests were conducted on both vitrimers after thermal healing at 100 °C for 24 h, and the corresponding stress–strain curves are presented in Fig. 6b. Optical images of the thermally healed films (Fig. 6a) confirmed that both vitrimers were successfully recovered, with no visible trace of the cut after healing.

After healing, both vitrimers exhibited stress–strain curves that closely followed their respective pre-healing curves, indicating a successful recovery of the network structure and tensile properties. To quantify the reprocessability, the values of each tensile property of the healed vitrimers were divided by their original numbers before healing and summarized as recovery ratios in Table 3. The BGF-based vitrimer exhibited superior reprocessability, as evidenced by its higher recovery ratios for E_t (∼88% *vs.* ∼69%), ε_b (∼87% *vs.* ∼66%), and σ_m (∼87% *vs.* ∼69%) compared to the BPF-based vitrimer. The enhanced healing efficiency of the BGF-based vitrimer can be attributed to its higher crosslink density, which increases the probability of dynamic bond exchange at the cut interface, facilitating bond reformation.[58] Another contributing factor to the better reprocessability of the BGF-based vitrimer could be its slightly lower weight loss during thermal healing, as suggested by an isothermal TGA measurement at 100 °C under air for 5 h,

Table 3 Recovery ratio of tensile properties for BPF- and BGF-based vitrimers after thermal healing at 100 °C for 24 h

Sample	Recovery ratio (%)		
	E_t	ε_b	σ_m
BPF-based	69 ± 6	66 ± 8	69 ± 2
BGF-based	88 ± 6	87 ± 2	87 ± 4

replicating the thermal healing conditions (Fig. S11†). The slight weight loss observed for both vitrimers (∼2% weight loss for the BPF-based vitrimer and ∼1% weight loss for the BGF-based vitrimer) likely also contributes to the incomplete recovery of tensile properties after healing. A separate thermal healing test with a shorter healing duration (1 h) is presented in Fig. S12,† and demonstrates significantly lower recovery for both vitrimers, highlighting the effect of healing time.

These findings underscore the potential for optimizing the healing protocol by adjusting factors such as applied pressure, healing time, and temperature. Nevertheless, the thermal healing experiments demonstrate that the proposed thiol-acrylate vitrimers can be readily healed under relatively mild conditions, offering a promising route for reprocessable material applications.

Conclusions

This work investigated the effect of structural differences in lignin-derivable (bis)phenols and their petroleum-based analogues on the network structure, mechanical properties, and bond exchange dynamics of thiol-acrylate vitrimers. The additional methoxy groups in the lignin-derivable vitrimer promoted intermolecular interactions during curing by acting as extra hydrogen-bonding acceptors. This enhanced interaction led to a network with higher crosslink density, as evidenced by the higher E'_r (∼2.4 MPa *vs.* ∼1.4 MPa) and T_g (∼34 °C *vs.* ∼28

°C) after thermal post-curing compared to its petroleum-based counterpart. Additionally, the lignin-derivable vitrimer exhibited a higher ε_b (~170% vs. ~130%) and improved mechanical robustness, achieving nearly twice the E_t (~6.9 MPa vs. ~3.4 MPa) and toughness (~750 kJ m^{-3} vs. ~390 kJ m^{-3}) due to its denser network structure. The higher crosslink density of the lignin-derivable vitrimer had an insignificant impact on bond exchange dynamics and reprocessability, as indicated by the similar stress relaxation behavior and E_a of viscous flow to the petroleum-based vitrimer. Furthermore, the lignin-derivable vitrimer demonstrated better recovery of tensile properties after thermal healing, potentially due to the denser network facilitating bond exchange events and its enhanced thermal stability, minimizing disruption of the network structure. This study herein established fundamental structure–property relationships by comparing these vitrimers with and without methoxy groups on the aromatic rings. The rapid UV curing capability of the thiol-acrylate reaction further showcases the versatility of these materials in manufacturing strategies. These features hold promise for potential biomedical applications, such as adhesives and dental materials, given by the abundance of hydroxyl groups, improved mechanical performance, and thermal healing ability with reduced estrogenic activity of the bio-derivable feedstocks. Overall, this work highlights the potential of lignin-derivable (bis)phenols in developing mechanically robust vitrimers toward addressing sustainability challenges in both feedstock sourcing and end-of-life management within the vitrimer design space.

Abbreviations

ATR-FTIR	Attenuated total reflectance-Fourier transform infrared
BAPO	Phenylbis(2,4,6-trimethylbenzoyl)phosphine oxide
BGF	Bisguaiacol F
BGFGA	Bisguaiacol F diglycidyl acrylate
BPA	Bisphenol A
BPF	Bisphenol F
BPFGA	Bisphenol F diglycidyl acrylate
CDCl$_3$	Deuterated chloroform
DMA	Dynamic mechanical analysis
DCM	Dichloromethane
DMSO-d_6	Deuterated dimethyl sulfoxide
DSC	Differential scanning calorimetry
E'	Storage modulus
E_a	Activation energy of viscous flow
E'_g	Storage modulus in the glassy state
E'_r	Storage modulus in the rubbery state
E_t	Young's modulus
ESI	Electrospray ionization
ε_b	Elongation-at-break
FTMS	Fourier transform mass spectrometry
GGA	Guaiacol glycidyl acrylate
HPPA	2-Hydroxy-3-phenoxypropyl acrylate
KOH	Potassium hydroxide
NaOH	Sodium hydroxide
NIR	Near infrared
NIPU	Non-isocyanate polyurethane
NMR	Nuclear magnetic resonance
PETMP	Pentaerythritol tetrakis(3-mercaptopropionate)
σ_m	Ultimate tensile strength
T_g	Glass transition temperature
TBAB	Tetrabutylammonium bromide
TGA	Thermogravimetric analysis
T_v	Topology freezing temperature
τ^*	Characteristic relaxation time
τ_0	Relaxation time prefactor

Data availability

The data supporting this article have been included as part of the ESI.†

Conflicts of interest

There are no conflicts of interest to declare.

Acknowledgements

References

1 A. M. Ortega, S. E. Kasprzak, C. M. Yakacki, J. Diani, A. R. Greenberg and K. Gall, *J. Appl. Polym. Sci.*, 2008, **110**, 1559–1572.

2 M. Podgórski, *J. Appl. Polym. Sci.*, 2009, **112**, 2942–2952.

3 C. Veith, F. Diot-Néant, S. A. Miller and F. Allais, *Polym. Chem.*, 2020, **11**, 7452–7470.

4 H. Fouilloux and C. M. Thomas, *Macromol. Rapid Commun.*, 2021, **42**, 2000530.

5 W. Post, A. Susa, R. Blaauw, K. Molenveld and R. J. I. Knoop, *Polym. Rev.*, 2020, **60**, 359–388.

6 D. E. Fagnani, J. L. Tami, G. Copley, M. N. Clemons, Y. D. Y. L. Getzler and A. J. McNeil, *ACS Macro Lett.*, 2021, **10**, 41–53.

7 Y. Liu, Z. Yu, B. Wang, P. Li, J. Zhu and S. Ma, *Green Chem.*, 2022, **24**, 5691–5708.

8 A. V. Krishnan, P. Stathis, S. F. Permuth, L. Tokes and D. Feldman, *Endocrinology*, 1993, **132**, 2279–2286.

9 N. Olea, R. Pulgar, P. Pérez, F. Olea-Serrano, A. Rivas, A. Novillo-Fertrell, V. Pedraza, A. M. Soto and

C. Sonnenschein, *Environ. Health Perspect.*, 1996, **104**, 298–305.

10 S. Takayanagi, T. Tokunaga, X. Liu, H. Okada, A. Matsushima and Y. Shimohigashi, *Toxicol. Lett.*, 2006, **167**, 95–105.

11 J. S. Mahajan, R. M. O'Dea, J. B. Norris, L. T. J. Korley and T. H. Epps, III, *ACS Sustain. Chem. Eng.*, 2020, **8**, 15072–15096.

12 R. M. O'Dea, J. A. Willie and T. H. Epps, III, *ACS Macro Lett.*, 2020, **9**, 476–493.

13 A. Vishtal and A. Kraslawski, *BioResources*, 2011, **6**, 3547–3568.

14 V. K. Thakur, M. K. Thakur, P. Raghavan and M. R. Kessler, *ACS Sustain. Chem. Eng.*, 2014, **2**, 1072–1092.

15 G. F. Bass and T. H. Epps, III, *Polym. Chem.*, 2021, **12**, 4130–4158.

16 P. J. De Wild, W. J. J. Huijgen and R. J. A. Gosselink, *Biofuels Bioprod. Biorefining*, 2014, **8**, 645–657.

17 W. Schutyser, T. Renders, S. Van den Bosch, S.-F. Koelewijn, G. T. Beckham and B. F. Sels, *Chem. Soc. Rev.*, 2018, **47**, 852–908.

18 K. H. Nicastro, C. J. Kloxin and T. H. Epps, III, *ACS Sustain. Chem. Eng.*, 2018, **6**, 14812–14819.

19 A. Amitrano, J. S. Mahajan, L. T. J. Korley and T. H. Epps, III, *RSC Adv.*, 2021, **11**, 22149–22158.

20 X. Zhang, J. S. Mahajan, L. T. J. Korley, T. H. Epps, III and C. Wu, *Mutat. Res. Toxicol. Environ. Mutagen.*, 2023, **885**, 503577.

21 X. Zhang, J. S. Mahajan, J. Zhang, L. T. J. Korley, T. H. Epps, III and C. Wu, *Food Chem. Toxicol.*, 2024, **190**, 114787.

22 S. V. Mhatre, J. S. Mahajan, T. H. Epps, III and L. T. J. Korley, *Mater. Adv.*, 2023, **4**, 110–121.

23 J. S. Mahajan, Z. R. Hinton, E. Nombera Bueno, T. H. Epps, III and L. T. J. Korley, *Mater. Adv.*, 2024, **5**, 3950–3964.

24 J. F. Stanzione, III, J. M. Sadler, J. J. La Scala, K. H. Reno and R. P. Wool, *Green Chem.*, 2012, **14**, 2346.

25 J. F. Stanzione, III, P. A. Giangiulio, J. M. Sadler, J. J. La Scala and R. P. Wool, *ACS Sustain. Chem. Eng.*, 2013, **1**, 419–426.

26 C. Zhang, S. A. Madbouly and M. R. Kessler, *Macromol. Chem. Phys.*, 2015, **216**, 1816–1822.

27 Y. Zhang, Y. Li, L. Wang, Z. Gao and M. R. Kessler, *ACS Sustain. Chem. Eng.*, 2017, **5**, 8876–8883.

28 Y. Zhang, Y. Li, V. K. Thakur, L. Wang, J. Gu, Z. Gao, B. Fan, Q. Wu and M. R. Kessler, *RSC Adv.*, 2018, **8**, 13780–13788.

29 A. W. Bassett, C. M. Breyta, A. E. Honnig, J. H. Reilly, K. R. Sweet, J. J. La Scala and J. F. Stanzione, III, *Eur. Polym. J.*, 2019, **111**, 95–103.

30 Y.-T. Wong and L. T. J. Korley, *Mater. Adv.*, 2024, **5**, 6070–6080.

31 C. Moretti, B. Corona, R. Hoefnagels, I. Vural-Gürsel, R. Gosselink and M. Junginger, *Sci. Total Environ.*, 2021, **770**, 144656.

32 Y. Luo, R. O'Dea, T. Epps, III and M. Ierapetritou, in *Computer Aided Chemical Engineering*, Elsevier, 2021, vol. 50, pp. 1683–1688.

33 Y. Luo, R. M. O'Dea, Y. Gupta, J. Chang, S. Sadula, L. P. Soh, A. M. Robbins, D. F. Levia, D. G. Vlachos, T. H. Epps, III and M. Ierapetritou, *Environ. Eng. Sci.*, 2022, **39**, 821–833.

34 T. Yan, A. H. Balzer, K. M. Herbert, T. H. Epps, III and L. T. J. Korley, *Chem. Sci.*, 2023, **14**, 5243–5265.

35 C. J. Kloxin, T. F. Scott, B. J. Adzima and C. N. Bowman, *Macromolecules*, 2010, **43**, 2643–2653.

36 C. N. Bowman and C. J. Kloxin, *Angew. Chem., Int. Ed.*, 2012, **51**, 4272–4274.

37 G. M. Scheutz, J. J. Lessard, M. B. Sims and B. S. Sumerlin, *J. Am. Chem. Soc.*, 2019, **141**, 16181–16196.

38 S. Maes, N. Badi, J. M. Winne and F. E. Du Prez, *Nat. Rev. Chem.*, 2025, **9**, 144–158.

39 W. Denissen, J. M. Winne and F. E. Du Prez, *Chem. Sci.*, 2016, **7**, 30–38.

40 N. J. Van Zee and R. Nicolaÿ, *Prog. Polym. Sci.*, 2020, **104**, 101233.

41 A. Kumar and L. A. Connal, *Macromol. Rapid Commun.*, 2023, **44**, 2200892.

42 W. Alabiso, T. M. Hron, D. Reisinger, D. Bautista-Anguís and S. Schlögl, *Polym. Chem.*, 2021, **12**, 5704–5714.

43 U. Shaukat, E. Rossegger and S. Schlögl, *Polymer*, 2021, **231**, 124110.

44 E. Rossegger, R. Höller, D. Reisinger, J. Strasser, M. Fleisch, T. Griesser and S. Schlögl, *Polym. Chem.*, 2021, **12**, 639–644.

45 A. Legrand and C. Soulié-Ziakovic, *Macromolecules*, 2016, **49**, 5893–5902.

46 Y. Liu, Z. Tang, Y. Chen, C. Zhang and B. Guo, *ACS Appl. Mater. Interfaces*, 2018, **10**, 2992–3001.

47 T. Isogai and M. Hayashi, *Macromolecules*, 2022, **55**, 6661–6670.

48 Y. Liu, Z. Tang, S. Wu and B. Guo, *ACS Macro Lett.*, 2019, **8**, 193–199.

49 J.-Q. Liu, C. Bai, D.-D. Jia, W.-L. Liu, F.-Y. He, Q.-Z. Liu, J.-S. Yao, X.-Q. Wang and Y.-Z. Wu, *RSC Adv.*, 2014, **4**, 18025–18032.

50 N. B. Cramer and C. N. Bowman, *J. Polym. Sci. Part Polym. Chem.*, 2001, **39**, 3311–3319.

51 M. Sahin, S. Ayalur-Karunakaran, J. Manhart, M. Wolfahrt, W. Kern and S. Schlögl, *Adv. Eng. Mater.*, 2017, **19**, 1600620.

52 S. Okamoto, T. Shinozuka and T. Endo, *Macromolecules*, 2021, **54**, 5806–5814.

53 L. Li, X. Chen, K. Jin and J. M. Torkelson, *Macromolecules*, 2018, **51**, 5537–5546.

54 M. Rubinstein, *Polymer Physics*, Oxford University Press, Oxford New York, 2003.

55 *The Physics of Rubber Elasticity*, ed. L. R. G. Treloar, Clarendon Press, Oxford New York, 3rd edn, 2005.

56 M. Sharifi, C. W. Jang, C. F. Abrams and G. R. Palmese, *J. Mater. Chem. A*, 2014, **2**, 16071–16082.

57 X. Zheng, Y. Guo, J. F. Douglas and W. Xia, *J. Chem. Phys.*, 2022, **157**, 064901.

58 M. Hayashi and R. Yano, *Macromolecules*, 2020, **53**, 182–189.

59 P. Miao, X. Leng, J. Liu, G. Song, M. He and Y. Li, *Macromolecules*, 2022, **55**, 4956–4966.